Interactive and Large-Domain Solutions of Higher-Order Viscous-Flow Equations

F. Stern,* S. Y. Yoo,† and V. C. Patel‡
University of Iowa, Iowa City, Iowa

Two approaches for the solution of the partially parabolic Reynolds equations are evaluated using the same numerical techniques and turbulence model. Comparisons are made between interactive viscous-inviscid solutions and noninteractive large-domain solutions for the flow over the tail and in the wake of axisymmetric and three-dimensional bodies to highlight the differences between the two strategies. Both approaches yield satisfactory results, although the interaction solutions appear to be computationally more efficient for the three-dimensional bodies.

Introduction

THE classical boundary-layer equations, which are based on the assumption that the viscous layer is thin relative to the local radii of curvature of the surface, are parabolic and neglect all influences of the downstream flow other than those contained in the inviscid-flow pressure field. Also, in the classical theory, the inviscid flow is calculated without accounting for the boundary-layer displacement effects. In spite of these approximations, there would seem to be no question as to the success of boundary-layer theory. The requirements of the theory are met in many practical flow situations and, for cases or flow regions in which they are not met, boundary-layer theory provides a formal framework upon which refinements and modifications can be applied and understood. However, the conditions of boundary-layer theory are not met in a variety of practical circumstances and, in these cases, some or all of the terms neglected in the Navier-Stokes equations to obtain the boundary-layer equations become important. For example, a review by Patel[1] of the experimental data for the flow over the tail and in the wake of axisymmetric and shiplike bodies points out the following features: 1) for many practical geometries, absence of flow reversal; 2) rapid thickening of the boundary layer; 3) variation of pressure across the viscous layer, implying strong viscous-inviscid interaction; 4) on three-dimensional bodies, development of a large longitudinal vorticity component; and 5) general reduction in the level of turbulence. Patel concludes that the appropriate governing equations for such viscous flows are the partially parabolic Navier-Stokes equations for laminar flow and the corresponding Reynolds equations for turbulent flow, hereafter referred to simply as the partially parabolic equations. There is, therefore, a need for approaches that solve these more general equations.

There are two possible approaches to the solution of the higher-order viscous-flow equations: a global approach, in which one set of governing equations appropriate for both the inviscid- and viscous-flow regions are solved using a large solution domain so as to capture the viscous-inviscid interaction; and an interactive approach, in which different sets of governing equations are used for each region and the complete solution obtained through the use of an interaction law, i.e., patching or matching conditions. The former approach is somewhat more rigorous because it does not rely on the patching conditions that usually involve further approximations. Nonetheless, for a variety of reasons, both types of approaches are of interest. A complete review of the vast literature in these two areas is beyond the scope of this paper. An overview is given, however, using selected references as examples for the purpose of putting the present work in perspective.

Traditionally, interaction studies have coupled the thin-boundary-layer equations with inviscid-flow solutions that include viscous-flow effects using either displacement-body or equivalent-source methods. Such methods have been successful in predicting flows for which the boundary-layer equations are, in fact, a good approximation in the viscous-flow region, e.g., thin airfoils and wings at small angles of attack. Extensions for thicker airfoils and wings and/or larger angles of attack, with limited regions of separation, have also been made. In these cases, the singularity of the boundary-layer equations at separation is removed by using the inverse mode, and single-pass solutions are obtained using the FLARE approximation. Here again, the results are satisfactory and, under most circumstances, the interactive procedures predict the flow as well as the global Navier-Stokes or partially parabolic Navier-Stokes solutions.[2,3]

Applications of direct- and inverse-mode interactive procedures to flows in which the boundary-layer equations do not represent a good approximation have generally had only limited success.[4-7] Investigations using higher-order equations for axisymmetric and three-dimensional bodies have been quite varied in the approximations embodied and turbulence models and numerical procedures utilized. Generally speaking, the results of most of these investigations have shown some improvement over the traditional interaction procedures; however, they do not show overall good agreement with the experimental data. Patel and Chen's[8] review of the extensive work on axisymmetric bodies indicates that this poor performance can be attributed to a variety of causes: lack of, incomplete, or incorrect viscous-inviscid interaction procedures; inconsistent approximations in the equations; poor accuracy and convergence of the velocity-pressure coupling procedures; turbulence modeling; and coordinates and grid dependence. Experience with three-dimensional bodies is much more limited, and few, if any, interactive solutions of higher-order viscous-flow equations have been attempted. In most cases, the outer boundary of the solution domain is placed at about two boundary-layer thicknesses from the body surface, where conditions are prescribed from the potential-flow solution without including the viscous-flow displacement effects. As pointed out by Chen and Patel,[9] much larger solution domains or interactive solutions are needed to capture the viscous-inviscid interaction.

Received March 23, 1987; revision received Nov. 17, 1987.

*Assistant Professor of Mechanical Engineering, Iowa Institute of Hydraulic Research.

†Graduate Research Assistant, Iowa Institute of Hydraulic Research; currently Research Scientist, Analytical Methods Inc., Redmond, WA.

‡Professor of Mechanical Engineering, Iowa Institute of Hydraulic Research. Associate Fellow AIAA.

The present paper is concerned with an evaluation of two approaches for the solution of the partially parabolic equations. Using the same numerical techniques and turbulence model, comparisons are made between viscous-inviscid interaction solutions and noninteractive large-domain solutions for the flow over the tail and in the wake of axisymmetric and three-dimensional bodies.

Interactive vs Noninteractive Solutions

Consider the flow past a streamlined three-dimensional body fixed in a uniform stream of velocity U_0. The classical approach to the analysis of such a flowfield is to divide it into three regions, as shown in Fig. 1, in each of which a different set of approximations is made in the Navier-Stokes (or Reynolds) equations. The resulting equations for the inviscid region 1 and the boundary-layer region 2 are well known. In the absence of flow reversal at the tail, the thick stern-flow boundary layer and the wake (region 3) can be described by the so-called partially parabolic equations, in which only the streamwise gradients of the viscous and turbulent stresses are neglected. The interaction (or lack of one) between regions 1 and 2 is the classical problem of boundary-layer theory. Herein, we are concerned with the flow in region 3 and its interaction with that in region 1.

Because the partially parabolic equations of region 3 also embody the inviscid-flow equations (and the boundary-layer equations), it should be possible to resolve the flow simultaneously in all regions by means of a single numerical solution of these general equations. In such a global, noninteractive approach, the solution domain must be large enough to apply uniform flow conditions at the far-field boundary S_O. Although this approach is feasible, it is generally believed to be less accurate and to be wasteful of computer time. One of the objectives of the present work is to investigate this aspect of the problem. An alternative approach is to seek separate solutions in regions 3 and 1 and match them iteratively at a common boundary Δ. As noted previously, such viscous-inviscid interaction techniques have been quite successful when the inner region obeys the boundary-layer equations, but there is little or no experience with interactive solutions of the more general partially parabolic equations. Another objective of the present work, therefore, is to investigate the feasibility of such solutions and compare the results of the two approaches with regard to accuracy and economy of computation.

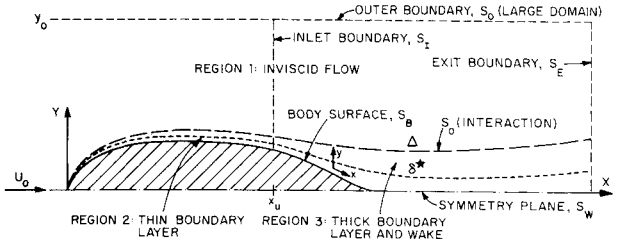

a) (X, Y) plane

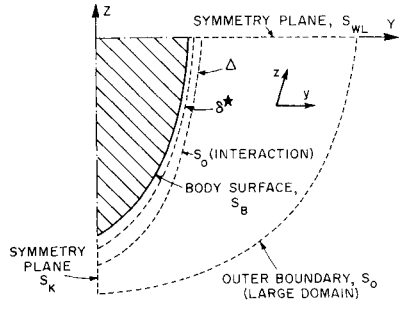

b) (Y, Z) plane

Fig. 1 Definition sketch of flowfield region.

The central problem addressed in this paper is the numerical solution of partially parabolic equations with two different outer boundary conditions, namely, the uniform-flow conditions appropriate for a noninteractive large-domain solution and the inviscid-flow matching conditions appropriate for an interactive solution. The details of this problem are considered in the next section. Unlike the large-domain solutions, the interactive solutions require specification of the match boundary Δ and an interaction law, along with a method for the calculation of the inviscid flow. In the present study, solutions were obtained both with the match boundary just beyond the boundary-layer thickness δ and with the boundary at about 2δ. The interaction law is based on the concept of displacement thickness. The displacement surface can be defined unambiguously by the following two requirements: 1) that it be a stream surface of the inviscid flow continued from outside the boundary layer, and 2) that the inviscid-flow discharge between this surface and any stream surface exterior to the boundary layer be equal to the actual discharge between the body and the latter stream surface. The second condition implies that the flow reduction inside the viscous flow is compensated for by an outward displacement of such a stream surface through a distance δ^*, i.e.,

$$\int_{A_{\delta^*}} \boldsymbol{V}_p \cdot \mathrm{d}\boldsymbol{A} = \int_{A_\delta} (\boldsymbol{V}_p - \boldsymbol{V}) \cdot \mathrm{d}\boldsymbol{A} \tag{1}$$

where $\boldsymbol{V}_p$ is the velocity vector of the outer inviscid flow continued into the viscous region, $\boldsymbol{V}$ is the viscous-flow velocity vector, and A_{δ^*} and A_δ are the cross-sectional areas between the actual body surface and the displacement-body surface and the boundary-layer surface, respectively. Thus, the inviscid-flow solution is obtained for the displacement body. This solution then provides the boundary conditions for the viscous flow:

$$U(\Delta) = U_p(\Delta) = U_e,\ W(\Delta) = W_p(\Delta) = W_e,\ p(\Delta) = p_p(\Delta) = p_e \tag{2}$$

Because δ^* and $\boldsymbol{V}_p(\Delta)$ are not known a priori, an initial guess must be provided and the complete solution obtained by iteratively updating the viscous- and inviscid-flow solutions until "patching" conditions 1 and 2 are satisfied. Note that, in this procedure, no assumptions have been made with regard to the thickness of the boundary layer.

In the inviscid-flow region (region 1 in Fig. 1), the flow is assumed to be irrotational. The boundary-value problem for the perturbation velocity potential is solved by a source-distribution method. The conforming panel, source-panel method of von Kerczek et al.[10] has been used. In this method, the integral equation for the source strength is solved by discretizing the body surface into a number of conforming surface panels, on each of which the source strength is assumed constant, and by evaluating the integral over each panel approximately by Gauss quadrature. The resulting system of linear equations is solved by Gauss-Seidel iteration. With the source strength known, the surface and field point velocities are readily calcu-

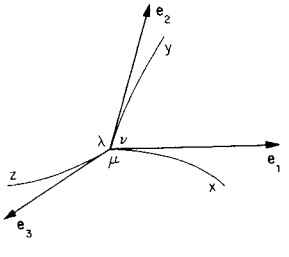

Fig. 2 Nonorthogonal curvilinear coordinates.

lated, again by Gauss quadrature, and the pressure is obtained from the Bernoulli equation. These procedures are facilitated through the use of a parametric surface equation to represent the body surface.

Solution of the Partially Parabolic Equations

For the thick boundary layer and wake (region 3 in Fig. 1), the governing equations are the partially parabolic equations. In these, the velocity field is elliptic in transverse planes and parabolic in the streamwise direction, while the pressure field is fully elliptic. Solutions to these equations can be obtained iteratively by solving the parabolic equations that result when the pressure field is specified and by subsequently updating the pressure field using the results from the parabolic solution. Of crucial importance is the manner in which the velocity and pressure fields are coupled. Many procedures have been tried for this purpose.[11] In the present work, a modified form of the SIMPLER algorithm,[12] which enhances global convergence,[9] has been used. Selection of an appropriate coordinate system and a grid-generation technique to obtain the coordinates is also important. A streamline coordinate system is the most consistent with the assumptions of the partially parabolic equations; such a system is difficult to generate, however, and may not be the most efficient from a numerical perspective. Alternatively, body-fitted coordinates can be used in which the axial coordinate is roughly aligned with the streamlines since they are coincident on the body surface itself. The partially parabolic assumptions are made in this preselected axial coordinate direction. In the present work, both simplified analytic and numerically generated body-fitted coordinates have been used. The Reynolds stresses are modeled using the k-ε turbulence model. A complete transformation of the governing equations is used such that the directions of the velocity components are along the grid lines. It should be recognized that very few investigators have used a complete transformation of the governing equations, especially for three-dimensional flows. The more common approach is a partial transformation, in which only the coordinates are transformed but the velocity components are maintained in either Cartesian or cylindrical coordinates. The governing equations are reduced to algebraic form using finite differences and are solved implicitly by the method of lines. In what follows, an overview of the equations and solution methodology is presented. The complete details are provided in Refs. 13 and 14.

Equations in Generalized Coordinates

The governing equations are solved in a nonorthogonal curvilinear coordinate system in which the x coordinate is roughly aligned with the flow direction and the y coordinate is in a plane transverse to the body axis X (Fig. 1a). For three-dimensional flow, the z coordinate is also in the transverse plane and in the girthwise direction (Fig. 1b). The Reynolds equations in nonorthogonal curvilinear coordinates can be derived either through the use of vector or tensor analysis. Here, we use the vector approach (see, e.g., Richmond et al.[15] for a derivation using tensors).

The momentum, continuity, and turbulence-model (k,ε) equations for steady incompressible flow can be written in the following vector form:

$$\nabla(\boldsymbol{V}\cdot\boldsymbol{V})/2 - \boldsymbol{V}\times\boldsymbol{\omega} = -\nabla(p/\rho) + \nu\{\nabla(\nabla\cdot\boldsymbol{V}) - \boldsymbol{V}\times\boldsymbol{\omega})\} - \nabla\cdot\overline{v_i v_j} + \overline{(v_i)\nabla\cdot\boldsymbol{v}} \tag{3}$$

$$\nabla\cdot\boldsymbol{V} = 0 \tag{4}$$

$$\boldsymbol{V}\cdot\nabla k = \nabla\cdot(\nu_t\nabla k)/\sigma_k + \tilde{G} - \varepsilon \tag{5}$$

$$\boldsymbol{V}\cdot\nabla\varepsilon = \nabla\cdot(\nu_t\nabla\varepsilon)/\sigma_\varepsilon + C_{\varepsilon 1}\tilde{G}\varepsilon/k - C_{\varepsilon 2}\varepsilon^2/k \tag{6}$$

where $\boldsymbol{V}=(U,V,W)$ are the mean velocity components, $\boldsymbol{v}=(u,v,w)$ are the turbulent fluctuations, p is mean pressure, $\boldsymbol{\omega}=\nabla\times\boldsymbol{V}$ is mean vorticity, $\overline{v_i v_j}$ are the Reynolds stresses (the overbar denotes time averaging), $k=\overline{\boldsymbol{v}\cdot\boldsymbol{v}}/2$ is turbulent kinetic energy, ε is turbulent energy dissipation, $\nu_t = C_\mu k^2/\varepsilon$ is eddy viscosity, and $\tilde{G}$ is turbulence generation. Because the fluid is assumed to be incompressible, the terms involving $\nabla\cdot\boldsymbol{V}$ and $\nabla\cdot\boldsymbol{v}$ in Eq. (3) are identically zero but have been included since they aid in putting the transformed equations into a more compact form. The usual values are used for the constants in the k-ε equations, namely, $(C_\mu, \sigma_k, \sigma_\varepsilon, C_{\varepsilon 1}, C_{\varepsilon 2}) = (0.09, 1.0, 1.3, 1.44, 1.92)$. The turbulence generation term is defined by

$$\tilde{G} = \nu_t[2(\varepsilon_{11}^2+\varepsilon_{22}^2+\varepsilon_{33}^2) + 4(\varepsilon_{12}^2+\varepsilon_{23}^2+\varepsilon_{31}^2)] \tag{7}$$

in which ε_{ij} is the rate-of-strain tensor

$$\varepsilon_{ij} = [\nabla\boldsymbol{V} + \nabla\boldsymbol{V}^T]/2 \tag{8}$$

$\nabla\boldsymbol{V}$ is the deformation-rate tensor e_{ij}, and $\nabla\boldsymbol{V}^T$ its transpose, i.e., $\nabla\boldsymbol{V}^T = e_{ji}$. The Reynolds stresses in Eq. (3) are related to k and ε through the isotropic eddy-viscosity concept,

$$\overline{v_i v_j} = -2\nu_t\varepsilon_{ij} + 2k(h_i h_j g_{ij})/3 \tag{9}$$

where the h_i are the metric coefficients and g_{ij} is the inverse metric tensor, both of which are defined later.

Equations (3–9) can be transformed into any coordinate system through the use of appropriate definitions of the gradient (∇), divergence ($\nabla\cdot$), and curl ($\nabla\times$) vector operators. The details of this procedure for orthogonal curvilinear coordinates are well known (e.g., Rouse[16]). For nonorthogonal curvilinear coordinates, the appropriate vector operator definitions are not readily available. They were probably first derived by Weatherburn.[17] Following Weatherburn, and referring to Figs. 1 and 2 for the present notation, the unit vectors $\boldsymbol{e}_i = (\boldsymbol{e}_1,\boldsymbol{e}_2,\boldsymbol{e}_3)$ in the directions of the nonorthogonal coordinates (x,y,z) are defined in terms of the Cartesian position vector

$$\boldsymbol{R} = X(x,y,z)\boldsymbol{i} + Y(x,y,z)\boldsymbol{j} + Z(x,y,z)\boldsymbol{k} \tag{10}$$

by

$$\boldsymbol{e}_1 = \boldsymbol{R}_x/h_1, \qquad \boldsymbol{e}_2 = \boldsymbol{R}_y/h_2, \qquad \boldsymbol{e}_3 = \boldsymbol{R}_z/h_3 \tag{11}$$

where

$$h_1 = |\boldsymbol{R}_x|, \qquad h_2 = |\boldsymbol{R}_y|, \qquad h_3 = |\boldsymbol{R}_z| \tag{12}$$

and a lettered subscript denotes a partial derivative. The angles (λ,μ,ν) between the (x,y,z) coordinate axes are given by

$$\cos\lambda = \boldsymbol{e}_2\cdot\boldsymbol{e}_3, \qquad \cos\mu = \boldsymbol{e}_1\cdot\boldsymbol{e}_3, \qquad \cos\nu = \boldsymbol{e}_1\cdot\boldsymbol{e}_2 \tag{13}$$

The inverse metric tensor is defined by

$$g_{ij} = (h_i\boldsymbol{e}_i\cdot h_j\boldsymbol{e}_j)^{-1} = \begin{bmatrix} AHG \\ HBF \\ GFC \end{bmatrix}/s \tag{14}$$

where

$$A = h_2^2h_3^2\sin^2\lambda,\ B = h_1^2h_3^2\sin^2\mu,\ C = h_1^2h_2^2\sin^2\nu$$
$$F = (h_1h_3\cos\mu)(h_1h_2\cos\nu) - h_1^2(h_2h_3\cos\lambda)$$
$$G = (h_1h_2\cos\nu)(h_2h_3\cos\lambda) - h_2^2(h_1h_3\cos\mu)$$
$$H = (h_2h_3\cos\lambda)(h_1h_3\cos\mu) - h_3^2(h_1h_2\cos\nu) \tag{15}$$

and s is the triple product

$$s = (h_1h_2h_3)(\boldsymbol{e}_1 \cdot \boldsymbol{e}_2 \times \boldsymbol{e}_3) = [Ah_1^2 + Hh_1h_2\cos\nu + Gh_1h_3\cos\mu]^{\frac{1}{2}} \tag{16}$$

In terms of the preceding quantities, the gradient of any scalar $Q(x,y,z)$ and the divergence and curl of any vector $\boldsymbol{V}(x,y,z) = V_1\boldsymbol{e}_1 + V_2\boldsymbol{e}_2 + V_3\boldsymbol{e}_3$ are given by

$$\nabla Q = \{(AQ_x + HQ_y + GQ_z)h_1\boldsymbol{e}_1 + (HQ_x + BQ_y + FQ_z)h_2\boldsymbol{e}_2 + (GQ_x + FQ_y + CQ_z)h_3\boldsymbol{e}_3\}/s^2 \tag{17}$$

$$\nabla \cdot \boldsymbol{V} = \left[\frac{\partial}{\partial x}(sV_1/h_1) + \frac{\partial}{\partial y}(sV_2/h_2) + \frac{\partial}{\partial z}(sV_3/h_3)\right]\Big/ s \tag{18}$$

$$\begin{aligned}\nabla \times \boldsymbol{V} = {} & \left\{\frac{\partial}{\partial y}[V_1h_3\cos\mu + V_2h_3\cos\lambda + V_3h_3] - \frac{\partial}{\partial z}[V_1h_2\cos\nu + V_2h_2 + V_3h_2\cos\lambda]\right\}h_1\boldsymbol{e}_1/s \\ & + \left\{\frac{\partial}{\partial z}[V_1h_1 + V_2h_1\cos\nu + V_3h_1\cos\mu] - \frac{\partial}{\partial x}[V_1h_3\cos\mu + V_2h_3\cos\lambda + V_3h_3]\right\}h_2\boldsymbol{e}_2/s \\ & + \left\{\frac{\partial}{\partial x}[V_1h_2\cos\nu + V_2h_2 + V_3h_2\cos\lambda] - \frac{\partial}{\partial y}[V_1h_1 + V_2h_1\cos\nu + V_3h_1\cos\mu]\right\}h_3\boldsymbol{e}_3/s\end{aligned} \tag{19}$$

The transformed equations (3–6) are very lengthy and are provided in Ref. 13. The equations have been put in a form similar to that used by Nash and Patel[18] for orthogonal curvilinear coordinates. A comparison shows that the coefficients in the equations in the nonorthogonal coordinates involve not only the curvatures of the coordinates but also their angular orientation.

The partially parabolic equations are obtained from the complete equations by using the following order-of-magnitude estimates: $(U,\partial/\partial x) \sim O(1)$; $(V,W,v_iv_j) \sim O(\delta)$; $(\partial/\partial y, \partial/\partial z) \sim O(\delta^{-1})$; $\nu \sim O(\delta^2)$; and $\delta \ll 1$. Patel[1] has shown that these are consistent with the partially parabolic assumptions. Also, in obtaining the partially parabolic equations, no assumptions are made with regard to geometrical quantities; that is, all geometrical quantities are considered $O(1)$. The x-momentum equation is obtained by retaining terms of $O(1)$ only. All other equations are obtained by retaining terms of $O(1) + O(\varepsilon)$. The partially parabolic equations are also provided in Ref. 13.

Discretization and Velocity-Pressure Coupling

The governing equations are reduced to algebraic form by approximating all the spatial derivatives by finite differences. A staggered-grid system has been used in order to facilitate the application of the velocity-pressure coupling procedure. The finite-difference scheme is basically only first-order accurate; however, certain derivatives have been evaluated using central differences, and all terms have been evaluated at the proper grid location by using averages of the surrounding values. The detailed finite-difference formulas are provided in Refs. 13 and 14. These then lead to the momentum and turbulence-model equations in the form,

$$a_1U^{\ell}_{m-1,n} + a_2U^{\ell}_{m,n} + a_3U^{\ell}_{m+1,n} = Su^{\ell}_{m,n} + Pu^{\ell}_{m,n} \tag{20}$$

$$b_1V^{\ell}_{m-1,n} + b_2V^{\ell}_{m,n} + b_3V^{\ell}_{m+1,n} = Sv^{\ell}_{m,n} + Pv^{\ell}_{m,n} \tag{21}$$

$$c_1W^{\ell}_{m,n-1} + c_2W^{\ell}_{m,n} + c_3W^{\ell}_{m,n+1} = Sw^{\ell}_{m,n} + Pw^{\ell}_{m,n} \tag{22}$$

$$d_1k^{\ell}_{m-1,n} + d_2k^{\ell}_{m,n} + d_3k^{\ell}_{m+1,n} = Sk^{\ell}_{m,n} \tag{23}$$

$$e_1\varepsilon^{\ell}_{m-1,n} + e_2\varepsilon^{\ell}_{m,n} + e_3\varepsilon^{\ell}_{m+1,n} = S\varepsilon^{\ell}_{m,n} \tag{24}$$

where (ℓ,m,n) are the grid point indices in the (x,y,z) directions, respectively, and $S\phi$ and $P\phi$, with $\phi = (U,V,W,k,\varepsilon)$, denote the source and pressure-gradient terms, respectively. Equations (20–24) are nonlinear since the coefficients a_i through e_i and the source terms are all functions of ϕ. If the pressure field is known, Eqs. (20–24) can be solved by the method of lines. However, because the pressure field is unknown, it must be determined such that the continuity equation is also satisfied.

The coupling of the velocity and pressure fields is accomplished through the use of a modified form of the SIMPLER algorithm. This is a two-step procedure in which, in the first step, the solution to the momentum equations for a guessed pressure field is corrected at each cross section such that continuity is satisfied. However, in general, the corrected velocities are no longer a consistent solution to the momentum equations for the guessed p. Thus, the pressure field must also be corrected. In the second step, the pressure field is updated again through the use of the continuity equation. This is done after a complete solution to the velocity field has been obtained for all cross sections. Repeated global iterations are thus required in order to obtain the converged solution. Both the pressure-correction and pressure equations have the same form and are derived in the same manner by substituting Eqs. (20–22) into the discretized form of the continuity equation (4) and representing the pressure-gradient terms by finite differences. The resulting equation for pressure involves 20 of the 27 nodes corresponding to all (x,y,z) indices $(\ell-1,\ell,\ell+1)$, $(m-1,m,m+1)$, and $(n-1,n,n+1)$, respectively; however, only certain terms are maintained to form a tridiagonal matrix, and all the remaining terms are grouped into a source term:

$$f_1p^{\ell+1}_{m,n} + f_2p^{\ell}_{m,n} + f_3p^{\ell-1}_{m,n} + f_4p^{\ell}_{m+1,n} + f_5p^{\ell}_{m-1,n} + f_6p^{\ell}_{m,n+1} + f_7p^{\ell}_{m,n-1} = Sp \tag{25}$$

Equation (25) is first used to correct the velocity field obtained from the solution of the momentum equations for a guessed pressure field. In this case, p is designated as $\hat{p}$, and both upstream and downstream values of $\hat{p}$ are neglected. Also, Sp is evaluated using the current solution to the momentum equations. The pressure-correction equation is solved at each cross section ℓ using the method of lines for two-dimensional and axisymmetric flows and an alternating direction implicit (ADI) method for three-dimensional flows. Subsequently, the velocity field is corrected using Eqs. (20–22) with $\hat{p}$ substituted for p and with the current solution to the momentum equations substituted for the neighboring velocities. When the exit cross section is reached, Eq. (25) is again used to update the pressure field. In this case, no approximations are made. The pressure equation is solved by marching from downstream to upstream using the method of lines for two-dimensional and axisymmetric flows and an ADI method for three-dimensional flows. With a new pressure field thus obtained, the entire process is repeated until the results converge; that is, when compatible velocity and pressure fields are found.

Solution Domains and Numerical Grids

The solution domains for both the large-domain and interaction solutions are shown in Fig. 1. It is seen that all boundary surfaces except the outer boundary are common to both methods. As discussed earlier, in the case of the large-domain solution, the outer boundary is placed far enough from the body to allow uniform-flow conditions to apply whereas, in the case of the interaction solution, the outer boundary is at the match

boundary Δ, with conditions specified from the inviscid-flow solution.

Two different grid-generation techniques have been used. For most of the small-domain interactive calculations, the match boundary is just beyond δ, and a simple analytic technique, in which local expanding grids for each cross section are pieced together (stacked) in the streamwise direction, has been used, i.e.,

$$x = X, y = \Delta y \delta(x,z)(\gamma_y^m - 1)/(\gamma_y - 1),$$
$$z = \Delta z \alpha(x)(\gamma_z^n - 1)/(\gamma_z - 1) \quad (26)$$

where Δy is the initial y-direction spacing, γ_y the expansion ratio in the y direction, Δz the initial z-direction spacing, γ_z the expansion ratio in the z direction, and $\alpha(x)$ the arc length of the body cross section. For the large-domain solutions, it was not possible to use such a simple analytic technique because, as the outer boundary is placed at greater distances from the body, this technique produces a grid in which the coordinates display humps and hollows near the body tail and midway across the flow domain. Consequently, for the large-domain solutions, the grids were obtained from Ref. 9. These were generated numerically from the solution of a set of elliptic partial differential equations. In one of the interactive calculations, a small-domain grid was obtained simply by deleting that portion of the large-domain grid that lay beyond about 2δ. This was done to evaluate the accuracy of the two approaches and to determine the effects of the placement of the outer boundary in the interaction solution. Typical large- and small-domain grids are shown in Fig. 3. Recall that, in the present approach, the velocity components are along these grid lines.

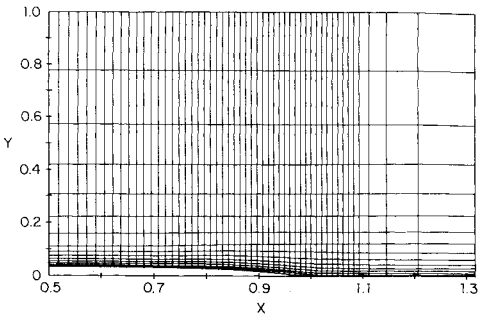

a) Large-domain grid: minor axis plane (partial view)

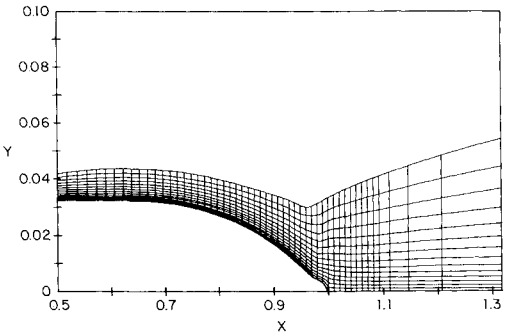

b) Small-domain grid: minor axis plane (partial view)

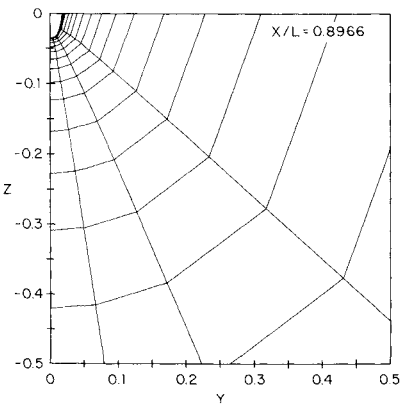

c) Large-domain grid: cross-sectional plane (partial view)

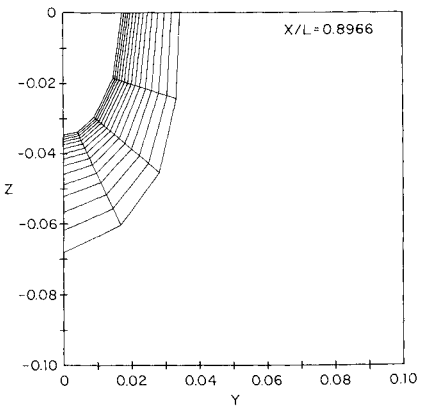

d) Small-domain grid: cross-sectional plane

Fig. 3 Grids for the 2:1 body.

Boundary Conditions

In terms of the notation for Fig. 1, the boundary conditions common to both the large- and small-domain solutions are as follows. On the inlet boundary S_I, the initial conditions for (U,V,W,k,ε) are specified from simple flat-plate correlations scaled to match the inviscid flow for $y \geq \delta$. Initial conditions for p and $\hat{p}$ are not required. Note that there can be differences between the initial conditions in the two solutions, depending on the specification of (U,V,W) for $y > \delta$ in the large-domain solution. In the large-domain solutions to be presented, the velocity components for $y > \delta$ were assumed to decay like the reciprocal of the distance squared from the values at $y = \delta$ to uniform-stream conditions. On the exit boundary S_E, a zero-gradient condition is used for p and $\hat{p}$; conditions for (U,V,W,k,ε) are not required. For laminar flow, the solutions are carried out up to the body surface S_B, where the no-slip condition is applied. For turbulent flow, the wall-function approach of Chen and Patel[9] is used. In this procedure, the first two grid points are placed in the log-law region. With a guessed value of the wall-shear velocity U_τ, the required boundary conditions at the first grid point for (U,V,W,k,ε) are obtained from the log-law and the assumption of local equilibrium. Because the log-law provides only the velocity magnitude, the velocity components are determined by assuming that the velocity vector in the (x,y) plane is parallel to the wall and in the (x,z) plane has the same direction as at the second grid point. After a field solution has been obtained, the solution at the second grid point is used to update the guessed value of U_τ, and the procedure is repeated until convergence. Conditions on p and $\hat{p}$ are not required on S_B. On the horizontal S_{WL} and vertical S_K symmetry planes, $\partial/\partial y(U,W,p,\hat{p},k,\varepsilon) = 0$, $V = 0$ and $\partial/\partial z(U,V,p,\hat{p},k,\varepsilon) = 0$, $W = 0$, respectively, are employed. As discussed earlier, both the location of the outer boundary S_O (see Fig. 1) and the conditions imposed thereon are different in the two solutions. In the large-domain solution, uniform-flow conditions, $(U,W,p) = (1,0,0)$, and $\partial/\partial y(k,\varepsilon,\hat{p}) = 0$, are specified. In the interaction solution, the edge conditions are specified

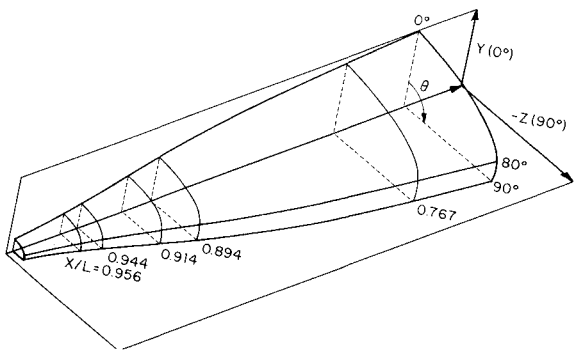

Fig. 4 DTNSRDC 2:1 elliptical cross-section body.

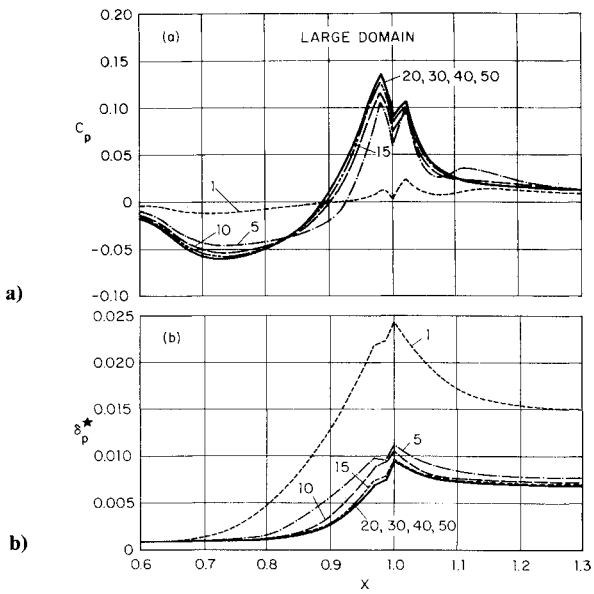

Fig. 5 Convergence history of the large-domain solution: a) pressure distribution on the surface of the body and along the wake centerline; and b) displacement thickness.

according to Eqs. (2): i.e., $(U,W,p) = (U_e,W_e,p_e)$ and $\partial/\partial y(k,\varepsilon,\hat{p}) = 0$, where (U_e,W_e,p_e) are obtained from the inviscid-flow solution evaluated at the match boundary Δ.

Turbulent Flow over Axisymmetric and Three-Dimensional Bodies

The two solution procedures described earlier were applied to calculate the thick stern boundary layer and wake of an axisymmetric and a simple three-dimensional body: namely, the David Taylor Naval Ship Research and Development Center (DTNSRDC) afterbody 1 and 2 : 1 elliptical cross-section body (see Fig. 4), for which experimental data were obtained by Huang and associates[4,6] (see Refs. 13 and 14 for other applications). The elliptical cross-section body has the same length and longitudinal distribution of cross-sectional area as the afterbody 1. The discussion of the results for the axisymmetric body will focus on the convergence characteristics of the two solutions whereas, for the three-dimensional body, a comparison is made between the converged results of the two solutions and also the experimental data. In the discussions to follow, all coordinates are nondimensionalized using the body length L, with $X = 0$ at the body nose, and velocities and pressure are normalized using the freestream velocity U_0 and the fluid density. The calculations were performed on a Prime 9950 minicomputer.

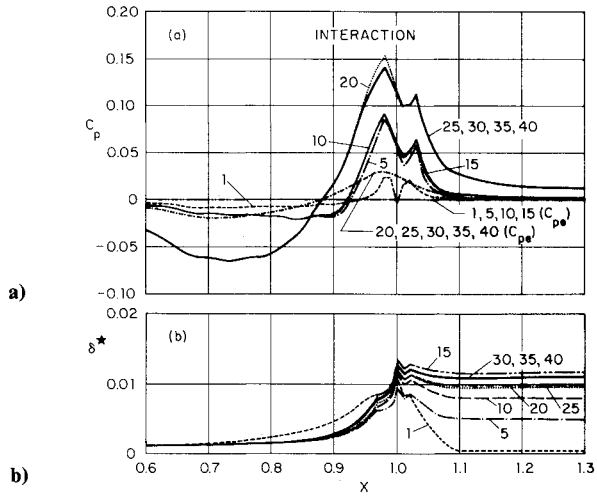

Fig. 6 Convergence history of the interaction solution: a) pressure distribution on the surface of the body and along the wake centerline, and on the match boundary; and b) displacement thickness.

Axisymmetric Body

The calculations for afterbody 1 were performed for a body-length Reynolds number $Re = 6.6 \times 10^6$, corresponding to the experiments. The large- and small-domain grids used in the calculations were similar to those for the minor-axis plane of the 2 : 1 body shown in Figs. 3a and 3b, respectively, which will be described later. Underrelaxation factors (α,α_p) were used in solving the momentum and pressure equations, respectively. For the large-domain solution, $(\alpha,\alpha_p) = (1,0.2\text{–}0.5)$ and, for the interaction solution, $(\alpha,\alpha_p) = (0.6,0.2\text{–}0.5)$. For both solutions, in the wake, $\alpha_p = 0.05$ for the first 10 global iterations, and $\alpha_p = 0.1\text{–}0.2$ for the subsequent global iterations until convergence was achieved.

Figures 5 and 6 show the convergence history with regard to the pressure distribution and the displacement thickness on the surface of the body and along the wake centerline for the large-domain and interaction solutions, respectively. Values are shown for every 5 global iterations. The large-domain solution converged in 50 global iterations and took 12 min of CPU time. The interaction solution converged in 40 global iterations and took 20 min of CPU time, of which 10 min were for the viscous-flow solution and 10 min for the inviscid-flow solution (2.5 min for each solution). The interaction calculations were started with freestream edge conditions $(U_e = 1, p_e = 0)$. Once partial convergence was achieved, which took 20 iterations, the edge conditions were updated using the latest value of displacement thickness. Subsequently, the edge conditions were updated every 5 global iterations until convergence was achieved. A comparison of Figs. 5 and 6 shows that the convergence characteristics of the two solutions are quite different. The large-domain solution converges monotonically in 50 iterations. The interaction solutions converge with oscillations in 40 iterations. Basically, the interaction solution converges in two stages. The first stage is with freestream edge conditions and leads to an underprediction of both C_p and δ^*. The second stage is with the displacement-body edge conditions, and the solution converges rapidly. Included in Fig. 6 is the iteration history of the edge pressure. The small changes in the displacement-body shape after 20 global iterations lead to imperceptible changes in p_e. Note that a planar definition of displacement thickness has been used for the large-domain solution as a result of difficulties in the evaluation of δ^* from Eq. (1) for the large-domain grid. Also, in evaluating Eq. (1) for the interaction solutions, the approximation V_p is constant across A_{δ^*} was used.

The converged results of the two solutions are compared with each other and with experimental data in Ref. 13. The

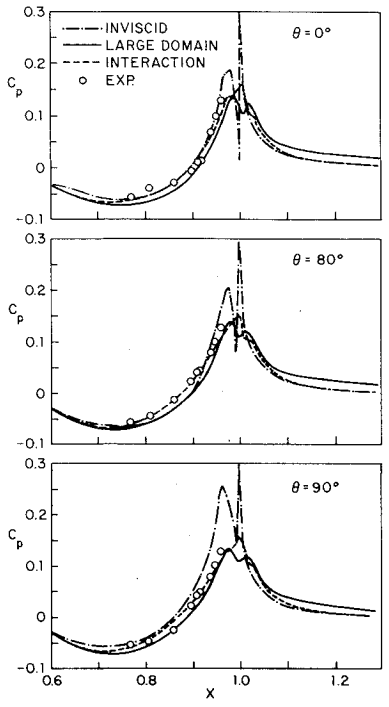

Fig. 7 Pressure distribution on the surface of the body and along the wake centerline.

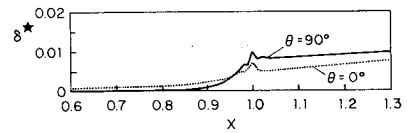

Fig. 8 Displacement thickness: interaction solution, minor and major axes planes.

characteristics of these comparisons are similar to those obtained for the 2:1 body discussed next.

Three-Dimensional Body

The calculations for the 2:1 body were performed for a body-length Reynolds number $Re = 6.5 \times 10^6$, corresponding to the experiments. The large- and small-domain grids used in the calculations are shown in Fig. 3. Figures 3a and 3b show the grids in the minor axis plane, while Figs. 3c and 3d show the cross-sectional views at $X = 0.8966$. The large-domain grid is $55 \times 18 \times 5$. The solution domain is bounded by the inlet S_I at $x_u = 0.5$, the exit S_E at $x_d = 2.5$, the outer boundary S_O at $y_O = 1.05$, the body surface, and the two planes of symmetry ($\theta = 0$ and 90 deg). The first grid point off the body surface was located in the range $150 \lesssim y^+ \lesssim 300$, where $y^+ = U_\tau y/\nu$. The small-domain grid is $55 \times 15 \times 5$. The inlet and exit boundaries, as well as the first grid point off the body surface, have the same values as in the large-domain grid, but the outer boundary is now placed at $y_0 = \delta$. The grid expansion was specified such that the first two grid points lie in the log-law region. An underrelaxation factor α_p was used in solving the pressure equation. For the large-domain solution, $\alpha_p = 0.2$–0.4 whereas, for the interaction solution, $\alpha_p = 0.3$–0.4.

The convergence characteristics of the solutions are similar to those described earlier for afterbody 1. The large-domain solution converged in 40 iterations and required 120 min of CPU time. The interaction solution converged in 30 iterations and required 90 min of CPU time. The interaction solution was started with freestream edge conditions. After 15 iterations, the edge conditions were updated using the latest displacement thickness. Subsequent updates of the edge conditions were not made. As shown earlier for afterbody 1, the small changes in displacement thickness after intermediate convergence is achieved (ca 15–20 iterations) lead to insignificant changes in the edge conditions. This was confirmed for the present application through numerical experimentation.

Next, a comparison is made between the converged results from the two methods and of both sets of results with the experimental data. Figure 7 shows the pressure distribution on the surface of the body and along the wake centerline for three girthwise positions $\theta = (0, 80, 90$ deg). It is seen that both methods are in good agreement with the experimental data. However, the interaction solution is in slightly better agreement. This is due to the influence of the initial conditions and the better grid resolution within the boundary-layer region for the interaction solution. A comparison of the present results with the inviscid-flow solution without interaction, which is also shown in Fig. 7, provides one indication of the magnitude of the viscous-inviscid interaction. This comparison is made somewhat difficult by the inaccuracy of the inviscid-flow solution very near the trailing edge. In the present inviscid-flow method, as is the case with most other singularity-distribution methods, the solutions are not accurate in regions where the angles between adjacent panels are small. This inaccuracy is well known and was not removed because the inviscid-flow solution without interaction is not used in the present viscous-inviscid interaction approach. The degree of viscous-inviscid interaction due to the stern boundary layer and wake for this body is similar in magnitude to that for the parent axisymmetric shape (afterbody 1), as seen by comparing Figs. 6 and 8. Figure 8 shows the final values of displacement thickness for the interaction solution for $\theta = 0$ and 90 deg. An approximate procedure was used to determine the displacement thickness $\delta^*(x,z)$: Eq. (1) was used along only the major and minor axes, with V_p assumed constant across A_{δ^*}, and these values were connected under the assumption that the displacement body is also elliptic in cross section. Note the larger viscous effects along $\theta = 90$ deg than along $\theta = 0$ deg in both Figs. 7 and 8.

Figure 9 shows the profiles of (U,V,W,C_p,k) at $X = 0.956$ (see Fig. 4). The radial coordinate is defined as $Y = (R - R_O)/R_{\max}$, where $R_O(x)$ is the local body radius, R the distance from the body surface along the local normal to the body cross section, and $R_{\max}$ the maximum value of the geometrical mean radius (i.e., the maximum radius of the afterbody 1). The calculated velocity components were interpolated and transformed into the experimental coordinate system in order to make the comparisons. The U component is in the axial direction, the V component in the direction of the local normal to the body cross section, and the W component orthogonal to both U and V. Consistent with the results discussed earlier, both solutions are in good agreement; however, some differences are evident, especially in the pressure. That is, whereas both solutions indicate similar transverse pressure gradients, there are systematic differences in pressure magnitude. The large-domain solution predicts lower pressure than the interaction solution which, in general, shows better agreement with the experimental data. A similar trend was found previously in the results for axisymmetric bodies. This may be related to the outer boundary conditions in the large-domain solution because its characteristics are similar to a blockage effect. The velocity components are in good agreement with the experimental data. This is especially true for the U component. The V component is slightly overpredicted. The W component is small and difficult to compare with the experimental values. The calculations show a systematic overprediction of the turbulent kinetic energy as the boundary layer thickens; namely, as the tail is approached and increasingly so towards $\theta = 90$ deg. Consistent with this, the calculated wall-shear stress indicates larger values than the experimental ones in the tail region ($x > 0.9$). These discrepancies are attributed to deficiencies of the k-ε turbulence model, which is known to over-

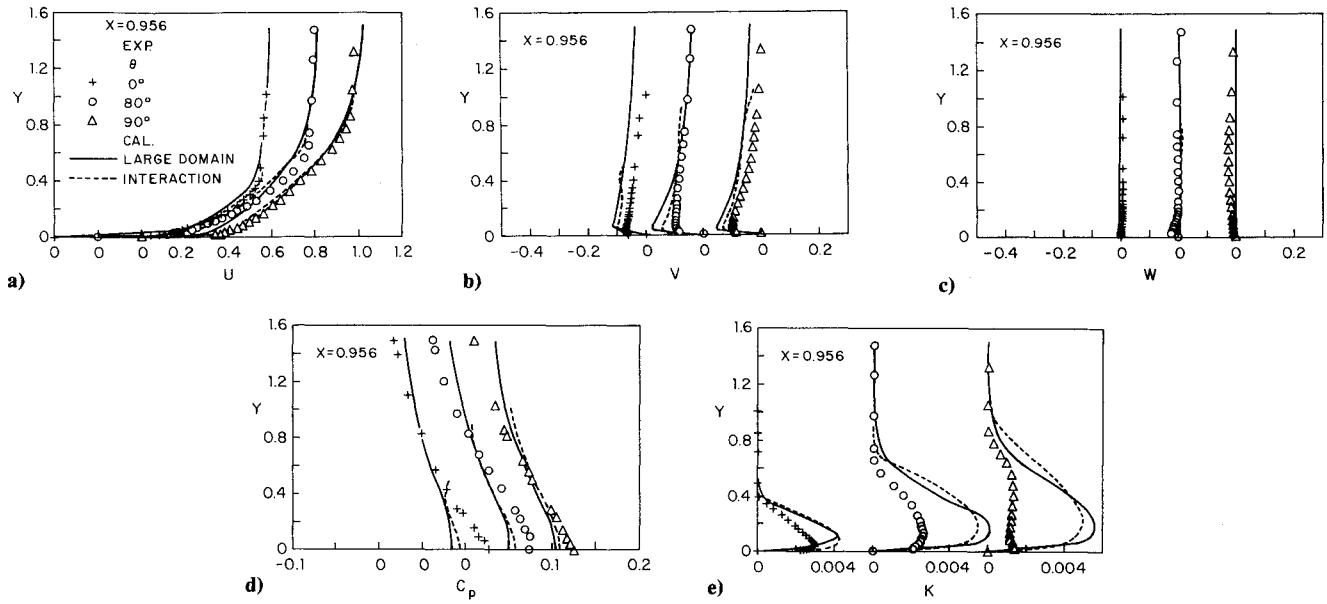

Fig. 9 Solution profiles.

predict the level of turbulence in thick boundary layers. Another cause may be the use of wall functions. Lastly, it is of interest to point out that the differences between the large-domain and interaction solutions are less pronounced when both methods use the same number and distributions of radial grid points within the viscous-flow region. This was demonstrated by the calculations for the 3:1 elliptic body described in Ref. 14.

Concluding Remarks

It has been shown that both large-domain solutions, in which the entire zone of viscous-inviscid interaction is captured, and small-domain interactive viscous-inviscid solutions yield satisfactory results for the flow over the tail and in the wake of axisymmetric and three-demensional bodies. Thus, both strategies are applicable to trailing-edge flows with thick boundary layers, and to similar complex turbulent shear flows, if all the important aspects of the flow, namely, pressure variation across the boundary layer and the displacement effect of the viscous flow on the external inviscid flow, are taken into account.

Comparison of the results from the present methods with those of other methods (see Ref. 13) and experimental data shows excellent agreement. Of particular interest is the comparison with the large-domain method of Chen and Patel[9] because their method and the present ones have certain features in common and are quite different in other respects. Specifically, the velocity-pressure coupling procedures, as well as the turbulence model, are similar; however, the coordinate systems used in solving the governing equations, the discretization procedures employed, and other numerical treatments are very different. Chen and Patel[9] and Patel and Chen[8] have presented results for the two bodies considered here, including comparisons with the same experimental data. The level of agreement is very similar to that shown with the present methods. Thus, it would seem that the most critical aspect of computational methods for thick-boundary-layer and trailing-edge flows is the velocity-pressure coupling rather than the discretization and numerical procedures employed.

As to the relative advantages of the interaction vs large-domain solutions, it appears that both lead to satisfactory solutions, indicating that the present viscous-inviscid interaction procedure is quite successful. The computational efficiency of the interaction solution depends both on the method used for the inviscid-flow solutions and the number of times the external flow is updated. That is, the overall efficiency is determined by the balance between the additional effort in calculating the inviscid flow and the savings in the viscous-flow calculations owing to the prescription of the inviscid flow at the match boundary, which accelerates convergence. In the present applications, the displacement-body method has been used, as opposed to the equivalent-source method. This is because the equivalent-source method is restricted to applications in which the body surface in the region of interaction has small curvature, e.g., airfoils and wings (see Ref. 13). For applications in which the equivalent-source method was used, the interaction solution was generally found to be more efficient than the large-domain solution.[13] This was also found to be true in previous investigations in which traditional interactive procedures were used.[2,3] For the applications in which the displacement-body method is used, however, as in the examples presented here, the large-domain solution is more efficient for the axisymmetric bodies, whereas the interaction solution is more efficient for the three-dimensional bodies (25% savings in overall CPU time for the cases considered). In the former cases, the inefficiency of the interaction solution can be attributed to the use of a three-dimensional method for calculating the inviscid flow and the updating of the inviscid-flow solution three times, which was probably unnecessary since the edge conditions showed no appreciable change.

Acknolwedgments

This research was sponsored by the Office of Naval Research, Accelerated Research Initiative (Special Focus) Program in Ship Hydrodynamics, under Contract N000-14-83-K-0136. The Graduate College of the University of Iowa provided a large part of the computer funds.

References

[1]Patel, V. C., "Some Aspects of Thick Three-Dimensional Boundary Layers," *Proceedings of the 14th ONR Symposium on Naval Hydrodynamics*, National Academy Press, Washington, DC, 1982, pp. 999–1040.

[2]McDonald, H. and Briley, W. R., "A Survey of Recent Work on Interacted Boundary Layer Theory for Flow with Separation," *Proceedings of the 2nd Symposium on Numerical and Physical Aspects of Aerodynamic Flows,* Session 5, Paper 1, California State Univ., Long Beach, CA, 1983.

[3]Mehta, V., Chang, K. C., and Cebeci, T. C., "Relative Advantages of Thin-Layer Navier-Stokes and Interactive Boundary Layer Procedures," NASA TM-86778, 1985.

[4]Huang, T. T., Santelli, W., and Belt, G., "Stern Boundary-Layer Flow on Axisymmetric Bodies," *Proceedings of the 12th ONR Symposium on Naval Hydrodynamics*, National Academy Press, Washington,

DC, 1978, pp. 127–157.

[5]Huang, T. T., Groves, N. C., and Belt, G., "Boundary-Layer Flow on an Axisymmetric Body with an Inflected Stern," David Taylor Naval Ship Research and Development Center, Bethesda, Md, Rept. 80/064, 1980.

[6]Huang, T. T., Groves, N. C., and Belt, G., "Stern Boundary-Layer Flow on Two Three-Dimensional Bodies Having Elliptical Transverse Cross-Sections," *Proceedings of the 2nd Symposium on Numerical and Physical Aspects of Aerodynamic Flows*, Session 10, Paper 2, California State Univ. Long Beach, CA, 1983.

[7]Piquet, J. and Visonneau, M., "Study of 3-D Ship Boundary Layers by Means of an Inverse Method," *Proceedings of the 4th International Conference on Numerical Ship Hydrodynamics*, National Academy Press, Washington, DC, 1985, pp. 529–542.

[8]Patel, V. C. and Chen, H. C., "Flow Over Tail and in Wake of Axisymmetric Bodies: A Review of the State of the Art," *Journal of Ship Research*, Vol. 30, No. 3, Sept. 1986, pp. 201–214.

[9]Chen, H. C. and Patel, V. C., "Calculation of Trailing Edge, Stern and Wake Flows by a Time-Marching Solution of the Partially-Parabolic Equations," Iowa Institute of Hydraulic Research, Univ. of Iowa, Iowa City, IIHR Rept. 285, April 1985.

[10]von Kerczek, C. H., Stern, F., Scragg, C. A., and Sandberg, W., "The Use of Theoretical and Computational Methods for Evaluating the Resistance of Appended Destroyer Hull Forms," Society of Naval Architects and Marine Engineers, Jersey City, NJ, Chesapeake Section Paper, Dec. 1983.

[11]Anderson, D. A., Tannehill, J. C., and Pletcher, R. H., *Computational Fluid Mechanics and Heat Transfer*, Hemisphere, New York, 1984, Chap. 8.

[12]Patankar, S. V., *Numerical Heat Transfer and Fluid Flow*, McGraw-Hill, New York, 1980, Chap 6.

[13]Stern, F., Yoo, S. Y., and Patel, V. C., "Viscous-Inviscid Interaction with Higher-Order Viscous-Flow Equations," Iowa Institute of Hydraulic Research, Univ. of Iowa, Iowa City, IIHR Rept. 304, Aug. 1986.

[14]Yoo, S. Y., Stern, F., and Patel, V. C., "Viscous-Inviscid Interaction with Higher-Order Viscous-Flow Equations: Applications to Three-Dimensional Bodies," Iowa Institute of Hydraulic Research, Univ. of Iowa, Iowa City, IIHR Rept. 307, March 1987.

[15]Richmond, M. C., Chen, H. C., and Patel, V. C., "Equations of Laminar and Turbulent Flows in General Curvilinear Coordinates," Iowa Institute of Hydraulic Research, Univ. of Iowa, Iowa City, IIHR Rept. 300, Feb. 1986.

[16]Rouse, H. et al., *Advanced Mechanics of Fluids*, Robert E. Krieger Publishing, Huntington, NY, 1976, Appendix A.

[17]Weatherburn, C. E., "On Triple Systems of Surfaces and Non-orthogonal Curvilinear Coordinates," *Proceedings Royal Society (Edinburgh)*, Vol. 46, 1926, pp. 194–205.

[18]Nash, J. F. and Patel, V. C., *Three Dimensional Turbulent Boundary Layers*, SBC Tech Books, Atlanta, GA, 1972, Chap. 2.